Acoustic Penetration of a Silty Sand Sediment in the 1–10-kHz Band

Nicholas P. Chotiros, Adrienne M. Mautner, Arne Løvik, Åge Kristensen, and Oddbjorn Bergem

***Abstract*—An experiment was performed to measure sediment penetrating acoustic waves to test a model of acoustic propagation, which is based on Biot's theory. Independent geophysical measurements provided model input parameters. A parametric sound source was used to project a narrow beam pulse into a silty sand sediment at a shallow grazing angle. The sediment acoustic waves were measured by an array of buried sensors and processed to measure wave directions and speeds. Two acoustic waves were observed, corresponding to the fast and slow waves predicted by Biot's theory. Discrepancies between model predictions and measured acoustic waves were examined, deficiencies in the model identified, and strategies for improvement postulated. The permeability and bulk modulus of the solid frame were of particular interest.**

***Index Terms*—Acoustic, penetration, permeability.**

I. Introduction

The LONG-TERM objective is to develop an acoustic model of ocean sediments that can accurately represent the physics of sound penetration into a wide variety of sediments. There are large acoustical differences between various types of ocean sediments, particularly in the transmission of sound from water into the sediment. In this paper, the emphasis is on the differences between sand and silt. Sand is a grain-supported structure that is controlled by mechanical forces at the grain-to-grain contacts, but silt tends to be a fluid-supported structure in which electrostatic forces between grains and fluid are dominant. A model is required that can smoothly make the transition from grain-supported to fluid-supported media and accurately represent the physics of acoustic penetration and propagation for any mixture of sand and silt.

The approach in this paper is to start with an existing baseline model that was developed for sandy sediments, to observe its performance when applied to a silty sediment, and then to attempt to formulate an improved model from the observations. This section provides a brief introduction to Biot's theory. In subsequent sections, the baseline model is described, followed by a description of the experiment and its results. The baseline model and experiment are compared and conclusions are drawn regarding the discrepancies and possible strategies for improvement.

Manuscript received June 19, 1996; revised April 2, 1997. This work was supported in part by the Office of Naval Research 321 OA under the Initiative for Research in Physics of Moderate to High Frequency Acoustics.

N. P. Chotiros and A. M. Mautner are with Applied Research Laboratories, The University of Texas at Austin, Austin, TX 78713-8029 USA.

A. Løvik, Å. Kristensen, and O. Bergem are with SACLANT Undersea Research Centre, 19026 La Spezia, Italy.

Publisher Item Identifier S 0364-9059(97)07959-4.

Acoustic wave equations are briefly reviewed below for the purpose of laying the foundation for the justification of using Biot's equations. The simplest wave equation is applicable to fluids

$$\mathbf{K}_b\nabla(\nabla\bullet\mathbf{u})=\rho\frac{\partial^2}{\partial t^2}\mathbf{u}\tag{1}$$

where ρ is mean density, $\mathbf{K}_b$ is bulk modulus, and $\mathbf{u}$ represents the displacement of the medium. Bold type is used to indicate complex quantities. For a lossy fluid, the bulk modulus $\mathbf{K}_b$ is a complex quantity, and its imaginary part represents the rate of loss of energy. The displacement $\mathbf{u}$ may be expressed in terms of a displacement potential Φ, and $\mathbf{K}_b$ is related to wave speed $\mathbf{s}$

$$\mathbf{u}=\nabla\Phi;\quad \mathbf{s}=\sqrt{\frac{\mathbf{K}_b}{\rho}}.\tag{2}$$

This equation has only one independent parameter, the sound speed $\mathbf{s}$, and it predicts just one compressional wave. The wave attenuation is represented by the imaginary part of the sound speed. In ascending order of complexity, the wave equation for an elastic solid is next:

$$\mu\nabla^2\mathbf{u}+(\mathbf{H}-\mu)(\nabla(\nabla\bullet\mathbf{u}))=\rho\frac{\partial^2}{\partial t^2}\mathbf{u}\tag{3}$$

where the displacement vector is expressible in terms of two potentials

$$\mathbf{u}=\nabla\Phi+\nabla\times\Psi.\tag{4}$$

This equation has one more parameter than the bulk wave equation, and it predicts two waves, a pressure and a shear wave. The term $\mathbf{K}_b$ in (1) has been replaced by $(\mathbf{H}-\mu)$. The second parameter is the shear modulus μ. In a lossy solid, usually referred to as viscoelastic, the independent parameters μ and $\mathbf{H}$ are complex quantities. These two wave equations have been used extensively to model acoustic interaction with the ocean sediment.

For a fluid-saturated porous elastic solid, wave propagation follows Biot's equations [1]. It consists of a pair of coupled equations describing the displacements of a porous solid frame $\mathbf{u}$ and a pore fluid $\mathbf{u}_f$. In practice, instead of $\mathbf{u}_f$, it is more convenient to describe the fluid displacement in terms of $\mathbf{w}$, the negative relative displacement of the pore fluid with respect to the frame weighted (by porosity). The equations are

$$\begin{aligned}\mu\nabla^2\mathbf{u}+(\mathbf{H}-\mu)(\nabla(\nabla\bullet\mathbf{u}))-\mathbf{C}(\nabla(\nabla\bullet\mathbf{w}))\\=\rho\frac{\partial^2}{\partial t^2}\mathbf{u}-\rho_f\frac{\partial^2}{\partial t^2}\mathbf{w}\end{aligned}\tag{5}$$

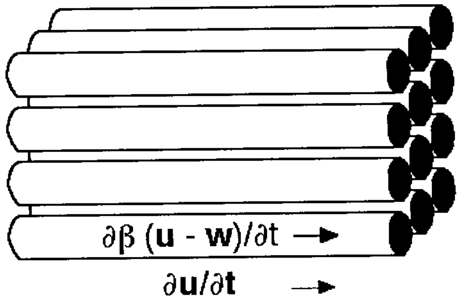

Fig. 1. Illustration of fluid-filled tubular pores in a solid matrix and the particle displacements modeled by Biot's equations.

$$\mathbf{C}(\nabla(\nabla \bullet \mathbf{u})) - \mathbf{M}(\nabla(\nabla \bullet \mathbf{w})) = \rho_f \frac{\partial^2}{\partial t^2}\mathbf{u} - \frac{c}{\beta}\rho_f \frac{\partial^2}{\partial t^2}\mathbf{w} - \frac{\mathbf{F}\eta}{\kappa}\frac{\partial}{\partial t}\mathbf{w} \quad (6)$$

where

$$\mathbf{w} = \beta(\mathbf{u} - \mathbf{u}_f). \quad (7)$$

Equation (5) is simply the wave equation of the uniform solid, (3), with two extra terms, one for the coupling between solid and fluid stresses involving the coupling coefficient $\mathbf{C}$ and the other for the coupling between the inertial forces. Similarly, (6) is the wave equation of a fluid, (1), with three additional terms to account for stress and inertial and viscous coupling with the solid frame. The displacement vectors may be expressed in terms of potentials

$$\mathbf{u} = \nabla\Phi_s + \nabla \times \Psi_s \quad \text{and} \quad \mathbf{w} = \nabla\Phi_f + \nabla \times \Psi_f \quad (8)$$

where the subscripts s and f refer to the solid frame and pore fluid, respectively. The medium is idealized as a collection of tubular pores in a solid matrix aligned with the direction of the compressional stress vectors, as illustrated in Fig. 1. The constants μ, $\mathbf{H}$, $\mathbf{C}$, and $\mathbf{M}$ on the left-hand side of (5) and (6) are constitutive coefficients that describe the elastic properties of the porous structure. On the right-hand side, ρ and ρ_f are the average and pore fluid densities, respectively. The constants β and η are frame porosity and fluid viscosity, respectively. The structure factor, c, and permeability, κ, provide inertial and drag corrections that compensate for the fact that, in practice, the pores are more tortuous than the simple model suggests. The term $\mathbf{F}$ represents a frequency-dependent drag coefficient. The above notation, which is different from the notation in the original derivation by Biot, is attributed to Stoll [2]. The solution, which may be found in a number of published sources [2]–[4], predicts two acoustic waves and one shear wave. The acoustic waves are commonly referred to as "fast" and "slow" waves. The solutions used here are from [4, eqs. (59) and (60)], after correction of typographical errors as listed in Appendix A.

Because the topmost layer of the ocean sediment consists of solid particles saturated with water, it is only natural that its behavior should be that of a water-saturated porous solid. Consequently, sound propagation may be expected to follow Biot's theory of acoustic wave propagation in a porous medium. Furthermore, there is evidence to indicate that Biot's theory is necessary to properly account for certain observed acoustic phenomena. Two phenomena are of particular importance: 1) acoustic penetration at subcritical grazing angles and 2) acoustic reflection loss. Sandy sediments tend to have sound speeds greater than that of water, and, by Snell's Law, a critical angle is predicted, below which no transmission through the water–sediment interface may be expected. Recent experimental results [5], [6] indicate significant subcritical grazing angle penetration, which is likely due to the slow wave predicted by Biot. It has also been observed that reflection loss at normal incidence over sandy sediments is greater than that predicted by the wave equations for either fluids or elastic solids of the same density and sound speed but is consistent with Biot's theory [7].

The disadvantage of Biot's theory is the large number of controlling parameters needed. These may be divided into two groups: the physical properties of the solid and fluid constituents and the dynamic properties of porous structure. The advantage is that Biot's equations can directly relate geophysical properties of the sediment, such as permeability, porosity, viscosity, and fluid density, to its acoustic properties, such as wave speeds and attenuations, in a physical way that is quite beyond the scope of the simpler wave equations.

II. Model of Acoustic Propagation

There are three parts to the model of sound propagation from water into sediment: the wave equations mentioned above, the boundary conditions at the interface, and the parameter values that the equations require.

Acoustic transmission through the water–sediment interface is governed by the usual boundary conditions. In the case of Biot's theory, there are up to six conditions [8]: continuity of normal and tangential stresses and displacements of the solid, and continuity of flow and pressure for the fluid. The boundary equation solutions already exist in a number of propagation models, including a fast field model[1] and a parabolic equation model [9]. The solutions used here are from [4, eqs. (55) and (56)], based on an original derivation by Stoll [8], and give the expressions for the displacement potentials of the solid and fluid constituents of the sediment. Particle velocities are computed from the time derivative of the gradient of the displacement potentials. Finally, acoustic pressure is computed from the product of particle velocity and impedance, averaged over the solid and fluid constituents.

Biot's equations require the values of a number of parameters, some of which are rather difficult to estimate, particularly the constitutive constants μ, $\mathbf{H}$, $\mathbf{C}$, and $\mathbf{M}$ and the permeability κ. The strategy is to estimate, as far as possible, the Biot parameters from a set of definitive, measurable quantities. The shear modulus μ may be inverted from shear wave speed; the imaginary part is adjusted to fit observed shear wave attenuation [10]. The constants $\mathbf{H}$, $\mathbf{C}$, and $\mathbf{M}$ are determined by the compressibilities of the pore fluid and the solid frame as measured by the jacketed and unjacketed tests; volumetric strain of the porous material, as defined

[1] OASES version 2.0, a fast field model for layered media, available from Prof. H. Schmidt, Massachusetts Institute of Technology, Cambridge.

by the volume within a membrane envelope, referred to as the jacket, is measured as a function of pore pressure and confining pressure [11]; the imaginary part of the jacketed bulk modulus, also known as the frame bulk modulus, is adjusted to fit observed attenuation of the fast wave. Permeability, κ, represents the ease with which fluids may flow through the pore spaces. For grain-supported structures, permeability, virtual mass parameter, and pore size may be estimated from the grain size distribution and porosity. Altogether, they form a procedure for estimating the Biot parameters from a set of definitive quantities. The details of such a procedure may be found in Chotiros [12]. This procedure, in combination with the solution of wave and boundary equations, constitute a baseline model of acoustic penetration into sandy sediments.

III. Input Parameters for This Experiment

Sediments with mean grain sizes between −1 and 4 ø are classed as sand [13], where ø is defined as minus log base 2 of the grain diameter in millimeters. Sediments with smaller grains are labeled as silt. The experiment took place in the Venere Azzura area off La Spezia, Italy, in a sediment of mean grain size 4.2 ø, which puts it at the borderline between sand and silt.

The definitive parameters for the baseline model were estimated as follows [12]. They may be divided into three groups: material properties of the solid and fluid constituents, fluid dynamics, and solid frame elasticity.

Pore fluid is salt water at 10 °C at a salinity of 35 ppt; its density is given by an empirical formula by Apel [14], and its bulk modulus computed from a formula for sound speed given by Medwin [15]. Visual analysis of the larger sediment grains showed mostly quartz and smaller proportions of carbonate grains and mica (plates). The smaller grains were mostly silt. The density of the solid grains was not measured but was estimated from historical information [16]; typical values lie between 2600 and 2800 kg/m^3. A value of 2700 kg/m^3 was assumed. The grain bulk modulus is not known. In Stoll's procedure, tabulated values for crystalline forms of similar materials were used, but no direct measurements were made until very recently, when the compressibility of a sample of quartz sand was measured [17]; a value of approximately 7 GPa was obtained, which is approximately a factor of 4 smaller than the tabulated value for quartz crystals. In the absence of any further information, 7 GPa was assumed. These values are shown in Table I.

Fluid dynamic parameters include viscosity, permeability, pore size, and virtual mass constant. The viscosity of sea water is slightly higher than that of fresh water due to dissolved salts, but the difference is very small, and its value may be approximated by that of fresh water [18]. The virtual mass constant was computed from porosity according to Berryman's procedure [19], which has been demonstrated to give results consistent with acoustic measurements on sintered glass beads. In a grain-supported structure, permeability and pore size may be estimated from porosity and the mean and standard deviation of grain size, assuming a normal distribution in ø space [12]. The cumulative grain size distribution, measured from diver-collected sediment samples, is shown in Fig. 2. For modeling purposes, a normal distribution was fitted to the points at values greater than 1%, which represent the vast majority of the grains, giving a mean and standard deviation of 4.2 and 0.26 ø, respectively. These were used to compute the permeability and pore size. The dashed curve, which represents a larger mean grain size, will be addressed later.

In this experiment, porosity and shear speed were not measured. This information was obtained from Richardson *et al.* [20], who measured grain size (2.6 to 4.2 ø), porosity (42 to 49%), and shear wave speed (60–100 m/s in the band 0.2–2 kHz) in the same area in 1990. Given the high correlation between grain size and porosity, and since the grain size at this site falls at the top end of the indicated range of the values measured by Richardson *et al.*, the porosity must also be at the top end of its range, i.e., 49%. The frame shear

TABLE I
Input Parameters for Sediment Acoustic Wave Propagation Model

Parameter	Value	Units	Reference
Grain size			
Mean	3.4	ϕ	Fig. 2
Standard deviation	0.6	ϕ	Fig. 2
Material properties			
Grain density	2700	kg/m^3	[16]
Grain bulk modulus	7.0E9	Pa	[17]
Pore fluid density	1028	kg/m^3	[14]
Pore fluid bulk modulus	2.28E9	Pa	[15]
Dynamic fluid properties			
Pore fluid viscosity	0.001	kg/m-s	[18]
Frame properties			
Porosity	0.49	—	[20]
Shear log derement	0.15	—	[10]
Bulk log decrement	0.15	—	[10]
Shear modulus	1.04E7	Pa	[20]
Bulk modulus	3.0E9	Pa	[21]

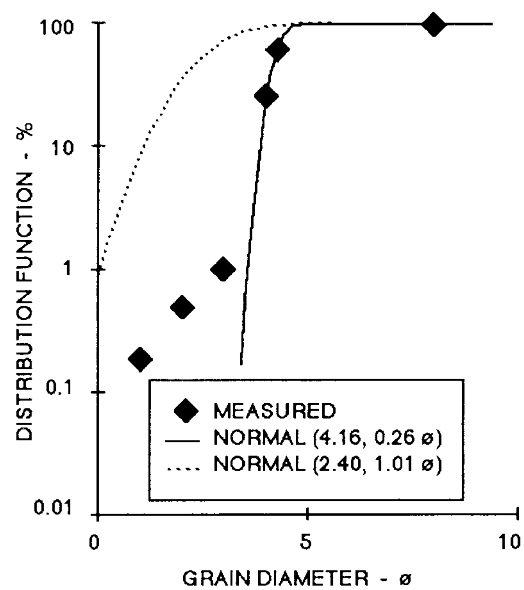

Fig. 2. Measured grain size distribution, best fit normal distribution used in the baseline model, and modified distribution to fit measured slow wave.

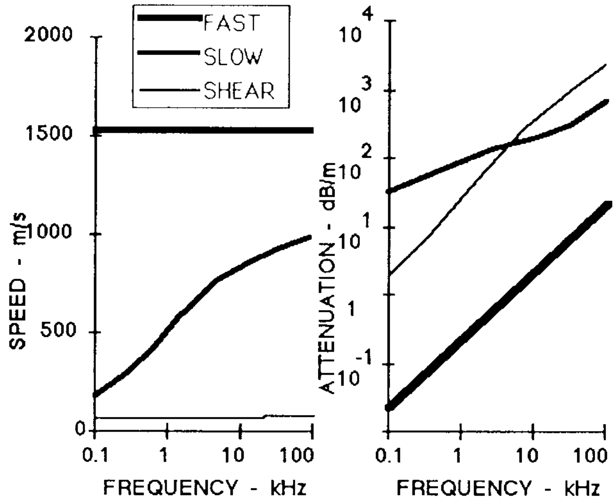

Fig. 3. Baseline model estimates of (a) speed and (b) attenuation of fast, slow, and shear waves as a function of frequency from parameter values in Table I.

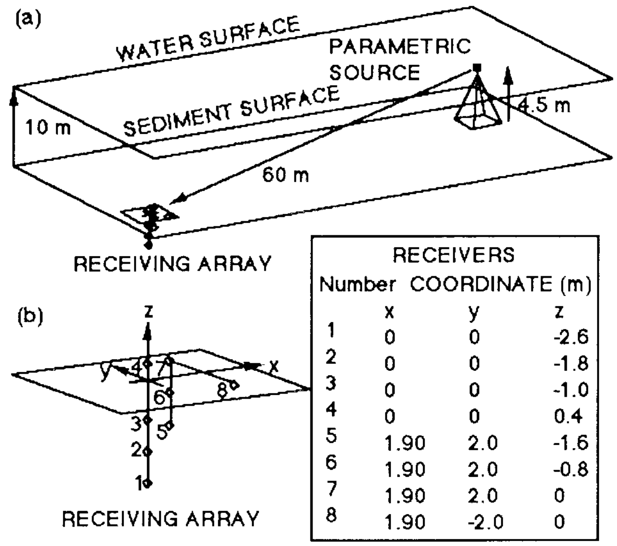

Fig. 4. Experiment configuration: (a) projection of sound pulse from a parametric source toward a buried receiving array and (b) buried array.

modulus was inverted from shear wave speed, which varied from 60 m/s at the sediment surface to 100 m/s at a depth of 0.6 m. Since the shear speeds were all very low, their effect on the acoustic wave speeds would be very small, and it should be adequate to approximate the shear modulus by a constant value corresponding to an average shear wave speed of 80 m/s. The bulk and shear log decrements were not measured. Stoll [10] estimated their values to be approximately 0.15 in the high-frequency regime.

The frame bulk modulus is the most difficult to estimate. It is normally inverted from the fast wave speed. From previously published measurements of near-surface fast wave speed as a function of mean grain size, as shown in [21, Fig. 7], the wave speed for a sediment of comparable grain size is expected to be approximately 1530 m/s. This value of fast wave speed was used to invert for the frame bulk modulus. All the input parameters in Table I, except the last, were applied to the solution of (5) and (6), and the fast wave speed was matched by adjusting the value of the frame bulk modulus; the resulting value is shown as the last entry in Table I.

The definitive set of parameters for the baseline model are now complete. They were applied according to the procedure developed for sandy sediments and the resulting speed, and attenuation of the fast, slow, and shear waves, as a function of frequency, are shown in Fig. 3. Above about 10 kHz, the wave speeds are predicted to settle about relatively constant values. At lower frequencies, there is a transition regime, in which the slow wave speed changes rapidly with frequency. This regime is of particular interest because it will severely test any model. The model is compared with experimental measurements as follows.

IV. Measurement of Sediment Acoustic Waves

A parametric source, the TOPAS PS040 made by Simrad, operating at a primary frequency of 40 kHz and generating a difference frequency signal in the water by self-demodulation, was used to direct a narrow beam and short pulse toward

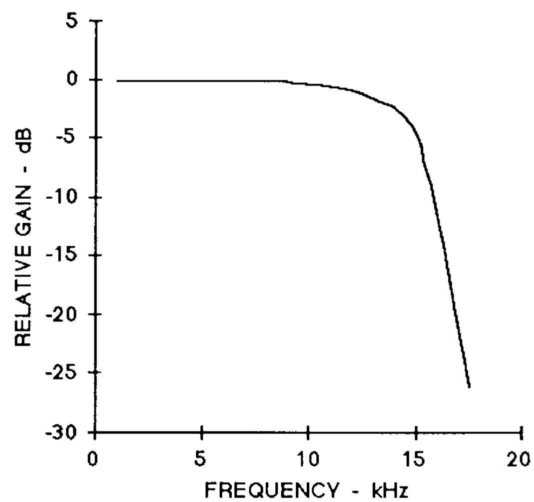

Fig. 5. Low-pass filter response.

a sparse three-dimensional (3-D) acoustic sensor array, as illustrated in Fig. 4. The parametric source was chosen for its narrow beam (3°), broad-band (1–20 kHz), and short-pulse-length (<0.5 ms) capabilities. It was mounted on a tower approximately 4.5 m high. The tower was stationary, but the direction of the sound beam could be steered. The receiving array was at a distance of 60 m from the source, in a water depth of 10 m. There were eight elements in the receiving array, of which two were on the sediment surface and one raised 0.4 m above it. The remainder of the receivers were buried in two vertical arrays. The transducers have a sensitivity of -201 ± 1 dB re 1 v/μPa in water. The preamps have a low-pass filter, which is 5 dB down at 15 kHz and rolls off sharply thereafter, as shown in Fig. 5.

The experiment took place in winter, in calm conditions and under overcast skies. Under such conditions, the temperature profile is known to be nearly isothermal, from historical information. In computing the sound speed in water, the temperature was estimated to be approximately 10 °C, and the salinity 35 ppt.

Accurate positioning of the array elements is essential for measurement of wave speed and direction. Positioning should be accurate to within a quarter of the acoustic wavelength. Uncertainty regarding the relative orientation and position of the sensor array and sound source position was resolved using the pulse arrival times at the surface hydrophones (4, 7, and 8). This permitted the horizontal positions of the surface hydrophones to be confirmed by time of flight measurements, and in some cases corrected, to the accuracy allowed by the leading edge of the acoustic pulse, which is approximately 1 cm. The positioning error in the two vertical buried line arrays may be estimated from the methods used to deploy them. The cables and hydrophones in each vertical line array were taped together to achieve the desired vertical separation; the accuracy is estimated to be about 1 cm. The bundle was stuffed into a flexible hose of approximately 5 cm in diameter. It is deployed in a bore hole that has a diameter of approximately 10 cm. The bore hole is initially supported by a sleeve. After insertion, the sleeve is withdrawn and the hole is allowed to collapse around the array. The worse possible error is determined by the diameter of the bore hole, less the diameter of the hydrophone, which gives a maximum horizontal positioning error of approximately ± 4 cm. For coherent signal processing, the error may not exceed one-quarter of a wavelength, therefore the minimum signal wavelength permissible is 16 cm. This will be referred to as the λ_{limit}.

V. Signal Processing

Coherent superposition is the principle underlying the method that is used to measure the speed and direction of acoustic waves. The processing is similar to that of a beamformer. Typically, a beamformer is used to determine the angle of arrival of one or more incoming signals. For broad-band signals, a time-delay beamformer is preferred over a phase-shift beamformer. A beamformer searches the range of possible angles to find the one that coincides with the arrival angle of the incident sound wave. Given that the wave speed is known, the process involves coherent addition of signals in such a way that a peak, proportional to the signal level, is obtained when the beam is pointed in the direction of the incident sound wave.

In this problem, both direction and speed of the incoming wave or waves are unknown. A process is needed that can search through a range of directions and speeds, and all combinations thereof, and produce a peak when the correct direction and speed is found. The signal processing steps are as follows: after digitization, the signal from each array element is multiplied by a weighting coefficient, Hilbert transformed to convert the series of real samples into complex samples, bandpass filtered to exclude unwanted signal and noise, time shifted to achieve the desired combination of beam angle and wave speed, and then coherently summed with corresponding signals from the other array elements. For equalization, the signal from each channel is weighted such that the integral of the voltage squared is normalized to a constant value. The signal from one of the sensors on the sediment surface is used as a timing reference. The intensity of the output is an indicator of the relative likelihood of the existence of a signal at a particular combination of beam angle and wave speed. The process is repeated until the entire search space of wave direction and speed combinations is covered. The process is illustrated in Fig. 6.

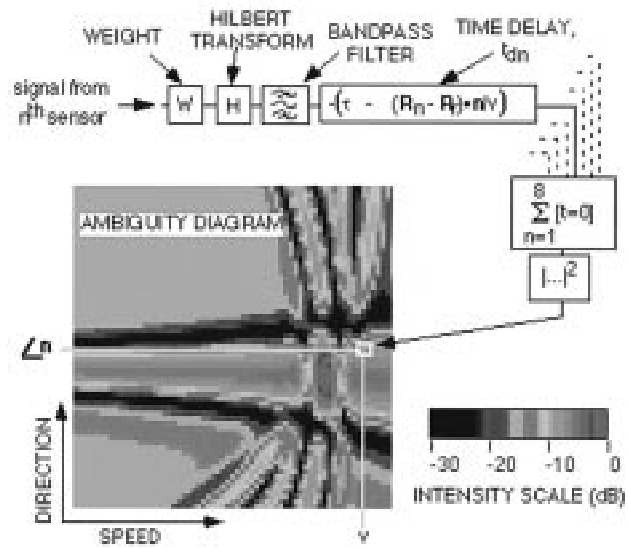

Fig. 6. Wave direction and speed estimation process.

In this case, the bearing of the source relative to the receiving array is known; therefore beam steering is needed only to cover all possible elevation angles in the vertical plane that cuts through the centers of both source and sensor array. The time shifting is based on an assumption of plane waves. Let t represent time, and let $t = \tau$ be the time at the peak of the signal from a designated reference sensor. For a combination of wave direction $\mathbf{n}$ and speed v, the time delay, t_{dn}, applied to the signal from the nth sensor is given by

$$t_{dn} = -(\tau - (\mathbf{R}_n - \mathbf{R}_r) \bullet \mathbf{n}/v) \tag{9}$$

where $\mathbf{R}_n$ and $\mathbf{R}_r$ are the vector positions of the nth and the reference sensors, respectively. The resulting signal at $t = 0$ is coherently summed, and its relative level, on a decibel scale, is plotted at the appropriate coordinate in a direction-speed space as a color-coded pixel. The scale is normalized such that the highest output is at zero decibels. The direction information resides in the unit vector $\mathbf{n}$, which, in this experiment, is simply the elevation angle of the acoustic wave. The process is repeated until the desired direction-speed search space is completely sampled. The resulting image may be called an ambiguity diagram. A peak will occur at the coordinates that match the angle and speed of an incoming wave.

More than one wave may be detected by this method because the process is linear up to and including the summation stage. The output from the summing operation is simply the superposition of the output signals of each wave. If their separation in speed or angle is greater than the resolution afforded by the array and the signal bandwidth, then, after

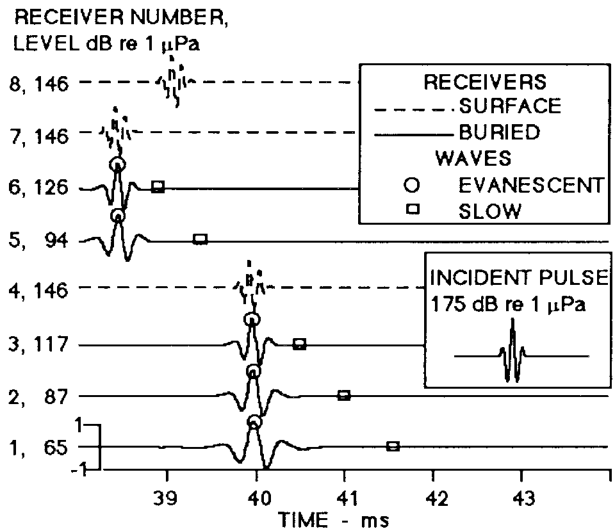

Fig. 7. Baseline model estimation of the pulses arriving at each receiver in response to a Ricker pulse.

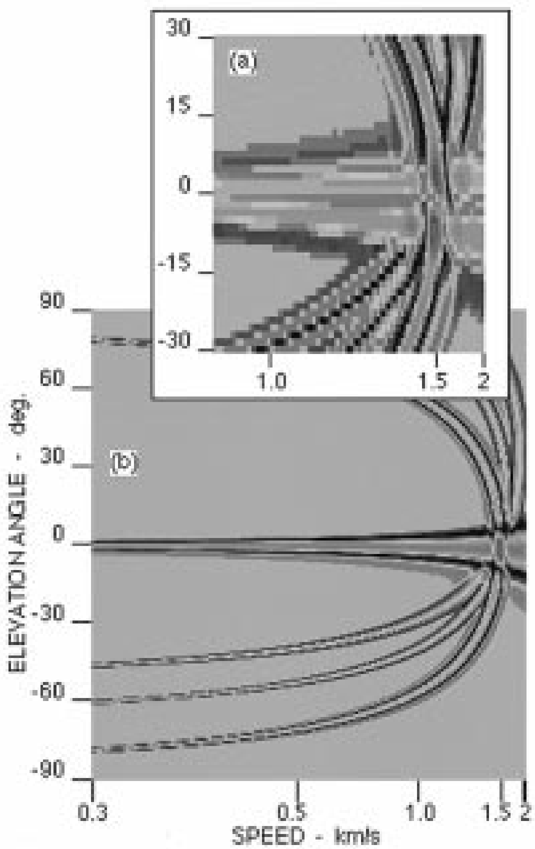

Fig. 8. Testing of wave speed and direction estimation process using baseline model generated signals of Fig. 7: (a) initial results and (b) after sign reversal of surface signals.

the square and log operations, each wave would produce a peak in a different part of the search space, with little mutual interference. The array was designed to maximize signal resolution in speed and angle.

The baseline model was used to compute the acoustic pressure signals at the eight receivers, in response to an incident plane wave pulse at 175 dB re 1 μPa and a grazing angle of 4.3°, as determined by the height of the projector and source–receiver separation. The signal is a Ricker pulse, which is typical of a pulsed parametric source. The acoustic pressures at each receiver are as shown in Fig. 7. The grazing angle is below critical for the fast wave; therefore it is evanescent. The evanescent and slow waves are marked for clarity, although the latter is too weak to be visible. As a test, the wave direction and speed estimation process was applied to these signals, and the resulting ambiguity diagram is shown in Fig. 8(a). The result should have been an evanescent wave traveling horizontally at a speed of 1493 m/s, but the diagram shows a split peak because there is a 180° phase shift between signals at the sediment surface and signals beneath the sediment surface. The phase reversal is quite evident in Fig. 7. Further simulations using the baseline model indicated that the phase reversal takes place over an interval of just a few centimeters below the sediment surface. To correct for this, the weights applied to all surface signals were negated. The corrected result is shown in Fig. 8(b), which shows the full search space of elevation angles from +90° (upward vertical) to −90° (downward vertical) and speeds from 300 to 2000 m/s. The peak at the correct speed and angle is clearly visible. In an effort to produce a plot that has constant resolution, the speed scale is inverted; i.e., the intervals of speed are of constant increments of 1/speed. This is because resolution is ultimately a function of time resolution, which is inversely proportional to speed. The width of each of the intersecting ridges in the ambiguity diagram is proportional to signal pulsewidth.

VI. Comparison of Theory and Experiment

Examples of signals recorded during the experiment are shown in Fig. 9. The elevation angle of the projector was adjusted to maximize the signal level at receiver 1, and then signals were recorded as the projector was slowly panned across the receiver array. The first arrival at each receiver is clearly recognizable. The reason it is labeled as "fast" rather than "evanescent" will be explained later. A number of other pulses arriving later are also evident, some of which are marked "slow," as will also be explained later.

The absolute value of the peak amplitude of each signal, based on receiving sensitivities in water, is shown along side the normalized wave. Evidently, the levels predicted by the baseline model are quite different from those measured in the experiment. In an effort to understand the cause of the discrepancies, the power spectra of certain signals were computed. Since the parametric source produces little energy below 1 kHz and the receiver has a flat response up to 12 kHz, only this band of frequencies is shown. In Fig. 10(a), the power spectra at the surface receivers show that model and experiment tend to agree at the high end of the band, but at the low end the experimentally measured levels were higher. At receiver 3, buried at a depth of 1 m, the measured signal spectrum is higher by 20 dB, but has the same shape as the baseline model, up to a breakpoint at around 7 kHz. Beyond the breakpoint, the gap widens, with the measured spectrum falling off at a much lower rate. Similar features are observed

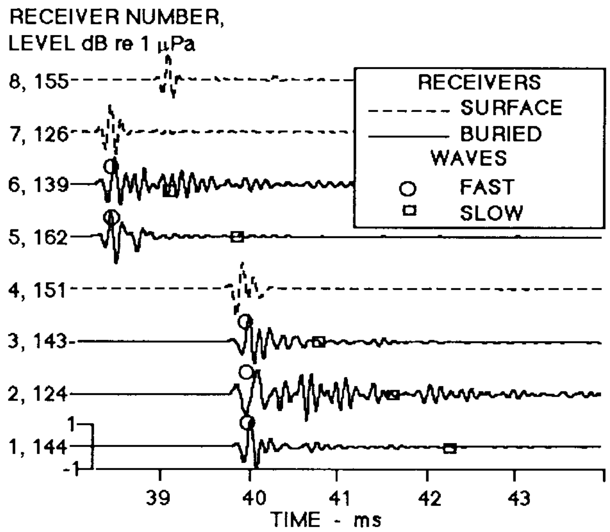

Fig. 9. Signals recorded at receiver array during the experiment.

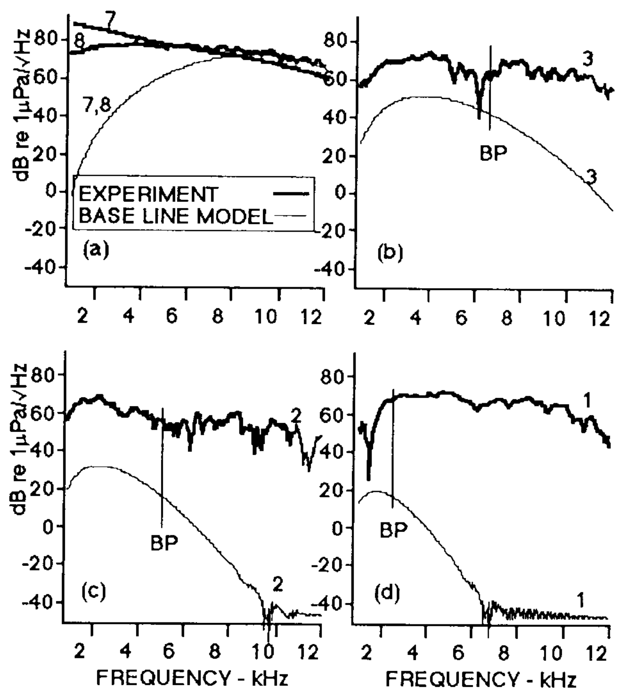

Fig. 10. Power spectral densities of the baseline and experimental signals at (a) receivers 7 and 8 on the sediment surface and at buried receivers (b) 3, (c) 2, and (d) 1.

at receivers 2 and 1, which are at depths 1.8 and 2.6 m, but with breakpoints at 5 and 3 kHz, and differences in level below the breakpoint of 30 and 40 dB, respectively. These results indicate that one or more frequency dependent effects in the experimental data are not represented in the baseline model.

Suspecting that there may be frequency dependence, we applied the wave speed and direction estimation process in discrete bands, approximately 2 kHz wide, and centered at 2, 4, 6, and 8 kHz. The results of processing both the baseline model generated waves of Fig. 7 and the experimentally measured signals in Fig. 9 are shown in Fig. 11. The ambiguity plots

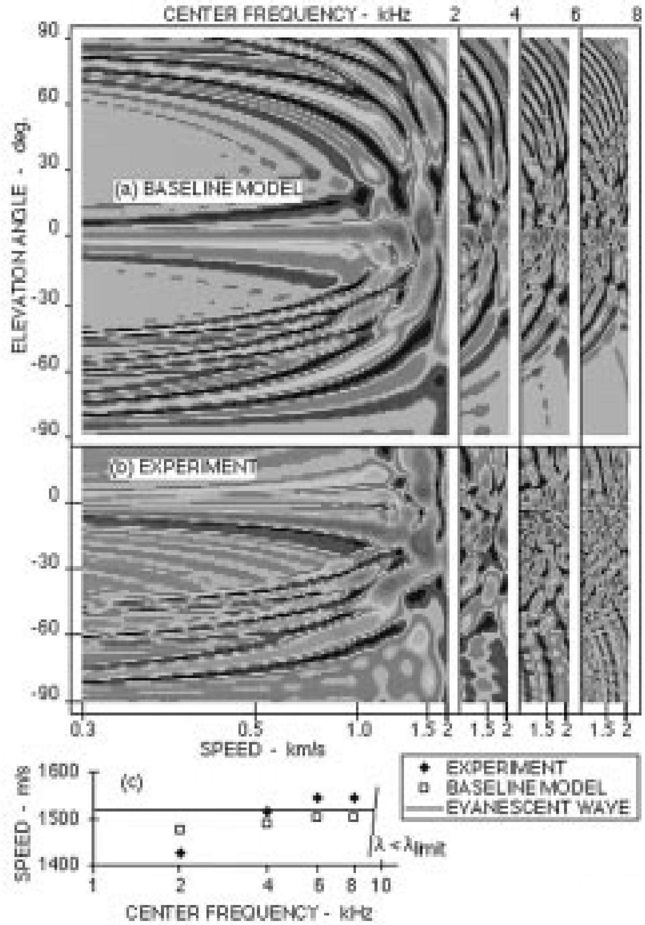

Fig. 11. Wave direction and speed ambiguity diagrams of (a) baseline model, (b) experimental signals, and (c) wave speed as a function of frequency up to the wavelength limit.

for each of the pass bands are stacked to highlight changes in the dominant wave as a function of frequency. It is evident that the sidelobes about the dominant peak become more numerous with increasing frequency. Although the usable band extends to 12 kHz, it was found that the dominant wave in the experimental data was not clearly discernible above 8 kHz. The reason is probably that above 8 kHz and at the fast wave speeds measured, the wavelength falls below the minimum (16 cm) permitted by receiver positioning accuracy. The minimum wavelength boundary is denoted by λ_{limit}.

At the estimated sound speed in water of 1489 m/s and a grazing angle of 4.3°, the evanescent wave is expected to be traveling horizontally, i.e., at an angle of 0° and at a speed of 1493 m/s. The ambiguity diagram generated from the baseline model shows a peak at a position very close to this angle and speed, in all the frequency bands. The experimental results, however, show a frequency-dependent result: at 2 kHz the indicated wave speed of 1426 m/s was slow enough to produce a refracted fast wave in the sediment, consistent with a downward angle of $-17°$ in accordance with Snell's Law. The wave speed appears to increase with frequency and level off at 1543 m/s at 6 kHz and above, but the indicated angles at the higher frequencies appear to be in violation of Snell's Law. This effect is a peculiarity of the parametric source and beyond the scope of the simple plane wave approximation used in the baseline model. The parametric source projects sound waves by nonlinear interaction of a high-intensity, high-frequency primary sound beam in the water. The source of the resulting secondary sound wave is not physically at the transducer but distributed as a virtual array in the water along the primary beam. When a parametric beam is directed toward the water–sediment interface at ranges comparable to or less than the length of the virtual array, penetration angles steeper than that allowed by Snell's Law have been observed experimentally by Muir *et al.* [22] and by Wingham *et al.* [23]; the latter also provided a theoretical model to support the experimental data. Theory and experiments show that the sediment penetrating wave is not an evanescent wave but is an acoustic wave propagating at its proper speed, which, in this case, is the fast wave. Of particular interest is the apparent frequency dependence of the fast wave speed. The baseline model, based on Biot's theory with constant coefficients, does not predict such a large frequency dependence.

The baseline model did not predict a detectable slow wave, but the experimental data showed numerous pulses after the initial fast wave arrival. The fact that the receivers on the sediment surface show only the first arrival and little else rules out the possibility of multipaths in the water column, such as the water surface bounce path. In any case, such multipaths are not expected because the parametric source has a conical beam width of only 3° with side lobe levels that are less than −30 dB. There is a possibility of volume scattering within the sediment, particularly at receivers 2 and 6, which have signals that show strong reverberation tails. That these scattering events are very localized suggests that the volume scatterers are similarly localized.

Scattering by surface roughness can produce an artifact having the appearance of a traveling wave at a speed c_a. The problem has been studied by Moe *et al.* [24]. Energy is scattered from surface roughness toward a buried receiver at the fast wave speed. The vertical component of phase speed is equal to the fast wave speed divided by the sine of the depression angle of the ray path. A minimum value of the pseudo wave speed c_m is obtained when the vertical phase speed is equal to the fast wave speed

$$c_a \geq c_m = \frac{c_f c_h}{\sqrt{c_f^2 + c_h^2}} \tag{10}$$

where c_f is the fast wave speed and c_h is the speed at which the scattered energy travels horizontally. The apparent ray angle θ is given by

$$\theta(c_m) = \tan^{-1}\left(\frac{c_h}{c_f}\right). \tag{11}$$

In a lossy medium, most of the energy arrives along the shortest path, which is vertically downward; therefore the vertical phase velocity tends to be equal to or only slightly greater than the fast wave speed. The horizontal phase velocity, c_h, should be treated as a variable. It is usually the speed of the evanescent wave along the sediment surface. This result has been corroborated by experimental observation in the laboratory by Simpson and Houston [25]. In general, c_h should be treated as a variable because energy may also be carried horizontally by any one of several interface waves.

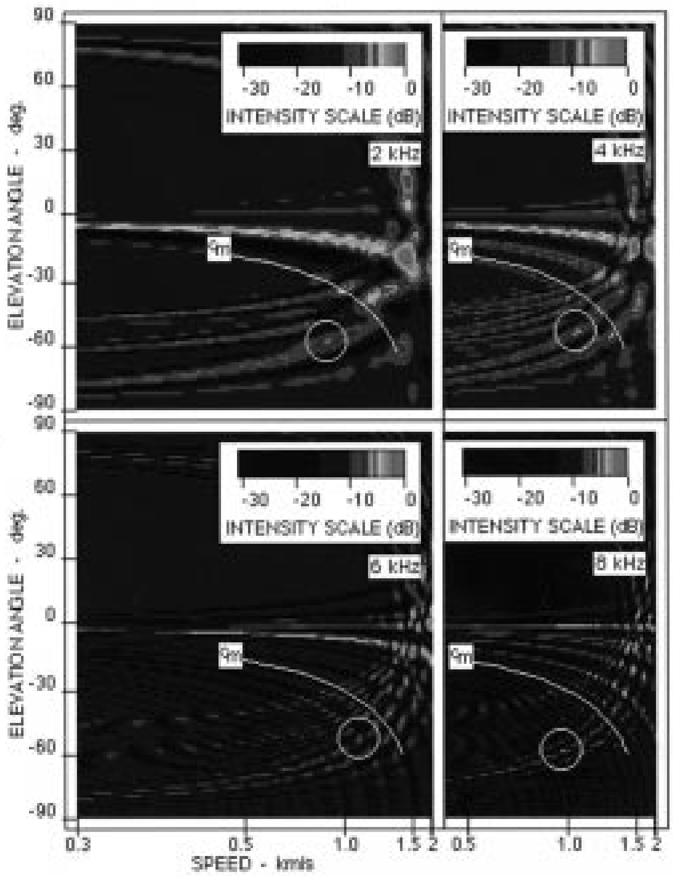

Fig. 12. Ambiguity diagrams of experimentally measured signals at 2, 4, 6, and 8 kHz with fine-tuned color palettes showing the minimum speed boundary of surface roughness scattered energy c_m and slow waves marked by circles.

There is also the possibility of another propagating wave hidden among the reverberation. For a better view, the color palettes of the experimentally measured ambiguity diagrams were adjusted for maximum sensitivity, as shown in Fig. 12. At each frequency, a curve is shown marking the minimum speed boundary c_m of the surface roughness scattered energy, as calculated from the measured fast wave speed and (10) and (11) for all likely values of c_h. Ambiguity peaks on the right of this curve are likely due to surface roughness scattering. To the left of c_m, at 2 kHz, an isolated peak is discernible at 760 m/s and −59°. Similar peaks are observable in the other frequency bands, as marked by circles. In each case, the strongest peak left of c_m was marked. The indicated wave speeds plotted against angle, as shown in Fig. 13, reveal that, except at 8 kHz, the speeds and angles are in excellent agreement with Snell's Law. The deviation at 8 kHz is most likely due to violation of the λ_{limit}, which occurs just above 6 kHz at these speeds. The wave speeds appear to increase steadily with frequency, from 760 to 969 m/s, and to show a much larger dispersion than the fast wave.

From the measured slow wave speeds, the approximate position of the slow wave was marked on the full-band time

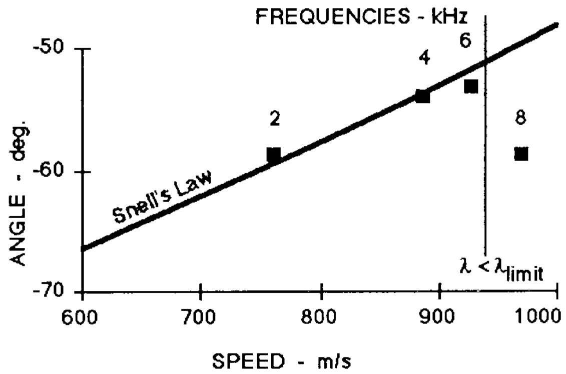

Fig. 13. Experimentally measured slow wave penetration angle as a function of speed and Snell's Law.

series from each buried receiver, as shown in Fig. 9. The position is only approximate due to the strong dispersion. The presence of a slow wave is not at all obvious from the time series, partly because it is masked by scattering and partly because of the smearing effect of the dispersion. Bandpass filtering reduced the detrimental effects of smearing, and coherent superposition raised the signal-to-background ratio to a level where a peak was just detectable in the ambiguity diagram. That these peaks are consistent with Snell's Law is indicative of a propagating wave. They are unlikely to be caused by roughness scattering because they are to the left of c_m. Finally, that they follow a consistent trend as a function of frequency makes it unlikely that they are caused by a random process but that they are manifestations of a slow, dispersive, and propagating wave.

Fast and slow wave attenuation were estimated, in each frequency band, by fitting a regression line through a plot of signal level, in decibels, as a function of path length, using signals from all the buried receivers. The standard error was estimated from the deviation of the data points from the regression line. The measured wave speeds and attenuations are compared with the baseline model, as shown in Fig. 14(a). The fast wave attenuation of the baseline model is within one standard deviation of the measured values, but the model is unable to match the measured frequency dependence of the fast wave speed. The greatest discrepancies are in the slow wave attenuation and speed. The speed trends are similar, but the measured values are significantly higher than the model. Although the measured attenuation of the slow wave comes with a large standard deviation, it is clearly an order of magnitude lower than that of the model.

Slow wave attenuation and to a lesser extent speed are most sensitive to permeability. In the baseline model, permeability is estimated from the grain size distribution and porosity values shown in Table I. The procedure was based on a grain-supported frame such as sand. In this case, the porosity is greater than that of a grain-supported frame. Rather than a random packing arrangement typical of sand, the structure may be flocculent, i.e., string-like structures separated by large pore spaces. Furthermore, the sediment is rich in nutrients and supports a variety of biological activity, so bioturbation may have generated even larger pore spaces. There are a few ways in

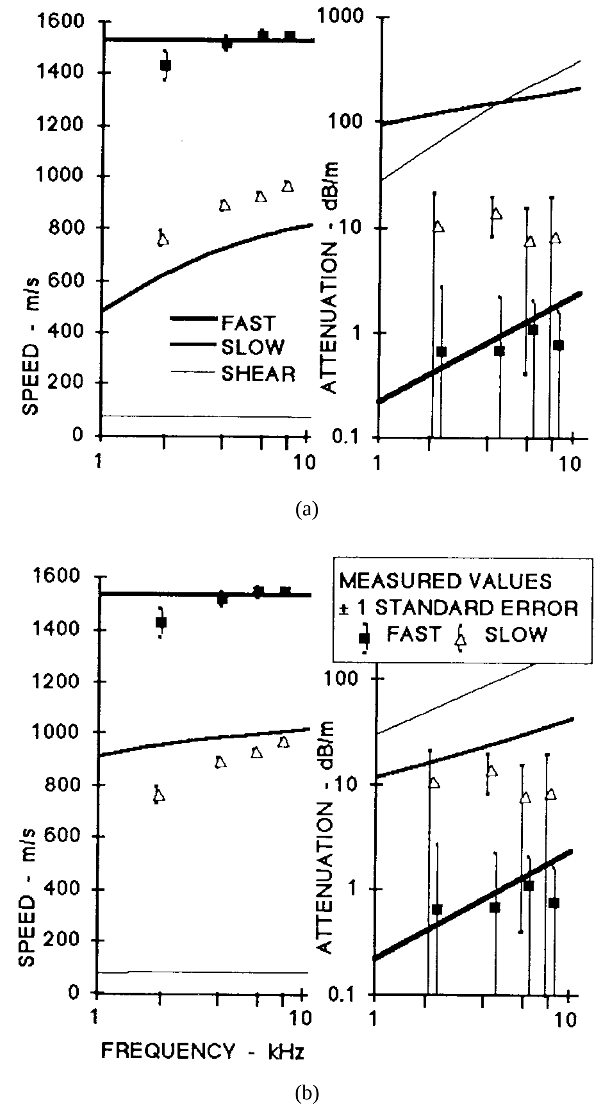

Fig. 14. Comparison of measured wave speeds and attenuations as a function of frequency with (a) baseline model and (b) baseline model with modified grain size statistics.

which this can happen. One is burrowing by biological organisms, which leaves tubular passages. Another is pelletization, which produces effectively larger grains. Certain organisms produce large quantities of mucous-encapsulated fecal pellets, which have been observed in soft sediments by Bentley *et al.* [26]. Pellet sizes are typically less than a millimeter. Such structures are not detectable by current methods of grain size analysis because solvents used to separate the grains would break up the flocculent structures, wash away the burrows, and dissolve the mucous encapsulations. It can be argued that the grain size measurement technique is unable to capture the effective *in situ* grain size distribution.

To some extent, the discrepancy may be alleviated by correcting the grain size distribution to properly reflect the effective, *in situ* grain size distribution, particularly resulting from pelletization. With reference to Fig. 2, the modified distribution function would lie to the left of the measured data points, signifying a wider range of larger grains. The two distributions should merge as the cumulative distribution approaches 100%. Within these constraints and still retaining a normal distribution model, the effect of a larger mean grain size was explored. This was done by varying the mean and computing a standard deviation that would intersect the measured distribution at the 99% level. It was found that as mean grain size was increased, the slow wave attenuation decreased and the speed increased, thus reducing both discrepancies. However, the speed over shot well before the attenuation discrepancy vanished. One of the better attempts was at a mean and standard deviation of 2.4 and 1.01 ø, as shown in Fig. 2. It gave slow wave speeds that were slightly higher than the measured value at 8 kHz and attenuations that were within a factor of 2 of the measured values, as shown in Fig. 14(b). Thus, to some extent, the discrepancy between model and experiment may be treated as a problem of estimating the correct, effective grain size distribution.

VII. Conclusion

The experiment may be summarized as follows. Bottom penetrating acoustic waves were launched by an incident sound pulse from a parametric source at a grazing angle of 4.3° and were received by a buried array of acoustic receivers in a silty sand sediment. The usable frequency band was limited by the low-frequency cutoff of the parametric source at 1 kHz and by the high-frequency cutoff of the receive system at 12 kHz. Within this band, errors in receiver positioning limited the effectiveness of coherent array processing to wavelengths greater than 16 cm.

The experiment was modeled using Biot's theory and a procedure for estimating the input parameters that was developed for sandy sediments, which is referred to as the baseline model. It predicted two acoustic waves and shear wave. The two acoustic waves are referred to as "fast" and "slow" waves. The incident sound wave at the water–sediment interface was modeled as a plane wave. The grazing angle was subcritical for the fast wave, making it evanescent. The model also indicated that the slow wave attenuation would be very high, rendering it undetectable.

The experimental results showed two waves. Although the model predicted that the fast wave would be evanescent, it was found propagating into sediment because of the unique ability of the parametric source to launch a wave at subcritical grazing angles. The violation of Snell's Law is only apparent because the incident wave is not a simple plane wave but a virtual array of sources distributed along the projected beam. Signals from the buried receivers showed a fast wave pulse followed by reverberation, which tended to obscure the slow wave trailing in its wake. With any one receiver, the slow wave could not have been detected with any confidence from among the reverberation. With coherent processing using all available receivers for maximum array gain and bandpass filtering to reduce the detrimental effects of dispersion, the slow wave was just detectable above the reverberation. The speeds and attenuations of both waves were measured as a function of frequency in 2-kHz bands, centered at 2, 4, 6, and 8 kHz.

There were discrepancies between baseline model and experiment in the attenuation of the slow wave and the speed of both waves. The baseline model predictions of slow wave speed and attenuation were too low and too high, respectively, most likely because the model underestimated sediment permeability. The model used a formula for estimating permeability based on a grain-supported frame, which is not entirely appropriate to a silty sediment. The structure of a silty sediment is more complicated than that of the randomly packed grains usually found in sand. The structure tends to be flocculent, which makes for larger pore spaces. Bioturbation tends to further increase permeability by the production of burrows and by pelletization. To some extent, the discrepancies between model and experiment may be treated as a problem in estimating the correct, effective grain size distribution. The discrepancies may be reduced by using a modified grain size distribution that better reflects the *in situ* structure of the sediment, particularly the pelletization. Other causes of discrepancy are likely to be in the calculation of the virtual mass constant and pore size parameter, both of which are computed on the basis of a grain-supported frame.

There was a discrepancy between model and experiment with regard to the frequency dependence of the fast and slow wave speeds. The baseline model, using constant input parameter values, was unable to reproduce the large dispersion found in the experimentally measured speeds. Therefore, certain parameters must be frequency dependent. The most likely candidate is the frame bulk modulus.

In conclusion, from a comparison of wave speeds and attenuations, between the baseline model and experiment, certain weaknesses in the model were evident, particularly the estimation of permeability, pore size, and virtual mass constant. In addition, the dispersion observed in both the fast and slow waves can be explained only in terms of frequency-dependent Biot parameters, and the most likely candidate is the frame bulk modulus. Starting at a baseline model developed for sandy sediments, these results will guide the development of an improved model that can smoothly make the transition from sandy to silty sediments and bring us closer to the goal of a model that can accurately represent the physics of acoustic penetration and propagation in a broad range of ocean sediments.

Appendix

Several equations in Stern *et al.* [4] have typographical errors. Of those, [4, eqs. (10), (11), (12), (34), (37), (53), (62), (63), and (64)] are relevant to this paper and to anyone who wishes to reproduce the acoustic model. The corrected equations are as follows:

$$\bar{K}_b = K_b(1 - i\delta/\pi) \tag{10}$$

$$\bar{\mu} = \mu(1 - i\delta_s/\pi) \tag{11}$$

$$\mu\nabla^2\mathbf{u} + (H - \mu)\nabla e - C\nabla\zeta = \rho\ddot{\mathbf{u}} - \rho_f\ddot{\mathbf{w}} \tag{12}$$

$$\psi_f = -\gamma\psi_s \tag{34}$$

$$\gamma = \rho_f\omega^2/(\bar{\rho}\omega^2 - \alpha) \tag{37}$$

$$\begin{aligned}\psi'_{s0} = {} & [-(i\rho\omega^2/2k\mu) + ik]\phi_{s0} \\ & + (i\rho_f\omega^2/2k\mu)\phi_{f0} + (i\rho_f\omega^2/2k\mu)(1 + R)\end{aligned} \tag{53}$$

$$D = \left\{ \frac{1}{4}\left(\kappa_s^2 + \kappa_f^2 + \frac{H\alpha}{d} - 2k^2\right)^2 - \left[\left(\kappa_s^2 - k^2\right)\left(\kappa_f^2 + \frac{H\alpha}{d} - k^2\right) + \lambda_f^2\left(-\lambda_s^2 + \frac{C\alpha}{d}\right)\right]\right\}^{1/2} \quad (62)$$

$$A_f = \left[\left(\kappa_s^2 - k^2 - \ell_1^2\right)/\left(-\lambda_s^2 - C\alpha/d\right)\right]A_s = \delta_1 A_s \quad (63)$$

$$B_f = \left[\left(\kappa_s^2 - k^2 - \ell_2^2\right)/\left(-\lambda_s^2 - C\alpha/d\right)\right]B_s = \delta_2 B_s \quad (64)$$

Acknowledgment

This was a joint experiment between ARL:UT and the SACLANT Centre for Undersea Research. The authors would like to acknowledge the crew of the RV *Manning* and the SACLANT Centre staff who carried out the experimental measurements. Sediment analysis at ARL:UT was by J. Piper. Particular recognition is due to the reviewers of the original manuscript, whose remarks have prompted significant improvements.

References

[1] M. A. Biot, "Theory of propagation of elastic waves in a fluid saturated porous solid," *J. Acoust. Soc. Amer.*, vol. 28, no. 2, pp. 168–191, 1956.

[2] R. D. Stoll, "Acoustic waves in ocean sediments," *Geophys.*, vol. 42, pp. 715–725, 1977.

[3] T. Yamamoto, "Acoustic propagation in the ocean with a poro-elastic bottom," *J. Acoust. Soc. Amer.*, vol. 73, no. 5, pp. 1587–1596, 1983.

[4] M. Stern, A. Bedford, and H. R. Millwater, "Wave reflection from a sediment layer with depth dependent properties," *J. Acoust. Soc. Amer.*, vol. 77, no. 5, pp. 1781–1788, 1985.

[5] R. A. Altenburg and N. P. Chotiros, "Plane-wave analysis of acoustic signals in a sandy sediment," *J. Acoust. Soc. Amer.*, vol. 89, no. 1, pp. 165–170, 1991.

[6] F. A. Boyle and N. P. Chotiros, "Experimental detection of a slow acoustic wave in sediment at shallow grazing angles," *J. Acoust. Soc. Amer.*, vol. 91, no. 5, pp. 2615–2619, 1992.

[7] N. P. Chotiros, "Inversion and sandy ocean sediments," in *Full Field Inversion Methods in Ocean and Seismic Acoustics, Conf. Proc. ISBN0-7923-3459-0*, The Netherlands, 1995.

[8] R. D. Stoll and T. K. Kan, "Reflection of acoustic waves at a water-sediment interface," *J. Acoust. Soc. Amer.*, vol. 70, pp. 149–156, 1981.

[9] M. D. Collins, W. A. Kuperman, and W. L. Siegmann, "A parabolic equation for poro-elastic media," *J. Acoust. Soc. Amer.*, vol. 98, pp. 1645–1656, 1995.

[10] R. D. Stoll, *Sediment Acoustics*. New York: Springer-Verlag, 1989.

[11] C. H. Yew and P. N. Jogi, "The determination of Biot's parameters for sandstones, Part 1: Static tests," *Experimental Mechanics*, pp. 167–172, May 1978.

[12] N. P. Chotiros, "Biot model of sound propagation in water-saturated sand," *J. Acoust. Soc. Amer.*, vol. 97, no. 1, pp. 199–214, Jan. 1995.

[13] J. E. Gillott, *Clays in Engineering Geology*. Amsterdam, The Netherlands: Elsevier, 1968.

[14] J. R. Apel, "Principles of ocean physics," in *International Geophysics Series*. New York: Academic, 1987, vol. 38.

[15] H. Medwin, "Speed of sound in water for realistic parameters," *J. Acoust. Soc. Amer.*, vol. 58, p. 1318, 1975.

[16] *Manual of Applied Geology for Engineers*, London, U.K.: Institution of Civil Engineers, 1976.

[17] J. C. Molis and N. P. Chotiros, "A measurement of grain bulk modulus of sands," *J. Acoust. Soc. Amer.*, vol. 91, no. 4, pt. 2, p. 2463, 1992.

[18] *American Institute of Physics Handbook*, 2nd ed. New York: McGraw-Hill, 1963.

[19] J. G. Berryman, "Elastic wave propagation in fluid-saturated porous media, II," *J. Acoust. Soc. Amer.*, vol. 69, no. 2, pp. 416–424, 1981.

[20] M. D. Richardson, E. Muzi, B. Miaschi, and F. Turgutcan, "Shear wave velocity gradients in near-surface marine sediment," *Shear Waves in Marine Sediments, Conf. Proc. ISBN0-7923-1357-7*, The Netherlands, pp. 295–304.

[21] E. L. Hamilton, G. Shumway, H. W. Menard, and C. J. Shipek, "Acoustic and other physical properties of shallow-water sediments off San Diego," *J. Acoust. Soc. Amer.*, vol. 28, no. 1, pp. 1–15, 1956.

[22] T. G. Muir, C. W. Horton, and L. A. Thompson, "The penetration of highly directional acoustic beams into sediments," *J. Sound Vib.*, vol. 64, pp. 539–551, 1979.

[23] D. J. Wingham, N. G. Pace, and R. V. Ceen, "An experimental study of the penetration of a water-sediment interface by a parametric beam," *J. Acoust. Soc. Am.*, vol. 79, no. 2, pp. 363–375, 1986.

[24] J. E. Moe, E. I. Thorsos, D. R. Jackson, and K. L. Williams, "The effect of roughness on acoustic penetration of the seafloor as given by a fluid-fluid perturbation model and comparison with recent sediment penetration experiments," *J. Acoust. Soc. Amer.*, vol. 97, no. 5, pt. 2, p. 3315, 1995.

[25] H. J. Simpson and B. H. Houston, "Measurement of acoustic wave speeds in a fluid-saturated sandy bottom," *J. Acoust. Soc. Amer.*, vol. 100, no. 4, pt. 2, p. 2766, 1996.

[26] S. J. Bentley, C. A. Nitrouer, and G. R. Lopez, "Measurement of progressive bioturbation in event layers, Eckernfrde Bay, southwestern Baltic Sea," in *Proc. Workshop on Modeling Methane-Rich Sediments of Eckernförder Bay*, Eckernförder, June 26–30, 1995.

Nicholas P. Chotiros received the B.A. degree in engineering from Trinity College, Cambridge University, England, and the Ph.D. degree in electronic and electrical engineering from the University of Birmingham, England, in 1973 and 1981, respectively.

He was a Faculty Member at the University of Birmingham, with teaching and research duties. Since 1982, he has worked at the Applied Research Laboratories, The University of Texas at Austin, on research projects in underwater acoustics, including nonlinear acoustics, sonar signal processing, and ocean sediment acoustics.

He is a fellow of the Acoustical Society of America and an associate member of the Institution of Electrical Engineers (U.K.).

Adrienne M. Mautner received the B.Sc. degree in mechanical engineering from the University of Texas at Austin in 1997.

From 1995 to 1997, she was a Laboratory Assistant and cooperative student intern in the Advanced Sonar Group of the Applied Research Laboratories, University of Texas at Austin. She is currently an Associate Design Engineer in the Piping Materials Group at Fluor Daniels, Sugarland, TX.

Arne Løvik was born in Bergen, Norway, in 1948. He received the M.Sc. degree and the Ph.D. degree in physical electronics from the University of Trondheim, Norway, in 1972 and 1980, respectively.

He has worked with underwater acoustic systems from 1972 within industry, applied research institutions, and universities. His present position is Head of the Minecounter Measures Group at the SACLANT Undersea Research Centre, La Spezia, Italy. His main areas of interest have been nonlinear acoustics, particularly the parametric array, fisheries acoustics, and high-resolution shallow seismic systems.

Åge Kristensen received the M.Sc. and Ph.D. degrees from the Institute of Technology, Trondheim, Norway, in 1976 and 1983, respectively.

During this time, he was employed in the Underwater Acoustics Group, Electronics Research Laboratory (ELAB), Trondheim, where he worked in sonar technology, hydroacoustic transducers, digital and analog electronics design and applications of acoustic methods in fisheries research. Since 1983, he has worked for the Petroleum Technology Research Institute, Trondheim (1983–1984), Southwest Research Institute, San Antonio, TX (1984), IKU, Trondheim (1985–1986), Statoil R&D Centre, Trondheim (1986–1990), all involving topics in borehole seismics, well logging instrumentation, and mathematical modeling of acoustic and electromagnetic wave propagation in boreholes. He was assigned to the SACLANT Undersea Research Centre, La Spezia, Italy, from 1990 to 1995 and was Head of the Seafloor Acoustic Group, involved in geophysical mapping of the upper sediments. He is currently Department Manager for Geophysics at Statoil R&D Centre.

Dr. Kristensen is a member of the Acoustical Society of America.

Oddbjørn Bergem received the M.Sc. degree from the Norwegian Institute of Technology in 1988 and the Ph.D. degree in the field of multibeam sonar processing from the University of Trondheim, Trondheim, Norway, in 1993.

From 1988 to 1994, he was employed at the Norwegian Defense Research Establishment, Division for Underwater Research, working on different projects related to high-frequency sonar processing. In August 1994, he joined the SACLANT Undersea Research Centre, La Spezia, Italy, where he is currently working as a Senior Scientist and project leader. His research interests include seafloor surface and volume scattering, seafloor classification, and high-frequency sonar processing in shallow water.

Dr. Bergem is a member of the Acoustical Society of America.